Zigzag magnetic order and possible Kitaev interactions in the spin-1 honeycomb lattice $KNiAsO_4$

K. M. Taddei,[1,*] V. O. Garlea,[1] A. M. Samarakoon,[2] L. D. Sanjeewa,[3,4,5,†] J. Xing,[5] T. W. Heitmann,[3] C. dela Cruz,[1] A. S. Sefat,[5] and D. Parker[5]

[1]*Neutron Scattering Division, Oak Ridge National Laboratory, Oak Ridge, Tennessee 37831, USA*
[2]*Materials Science Division, Argonne National Laboratory, Lemont, Illinois 60439, USA*
[3]*University of Missouri Research Reactor, University of Missouri, Columbia, Missouri 65211, USA*
[4]*Department of Chemistry, University of Missouri, Columbia, Missouri 65211, USA*
[5]*Materials Science and Technology Division, Oak Ridge National Laboratory, Oak Ridge, Tennessee 37831, USA*

(Received 21 September 2022; revised 15 November 2022; accepted 14 December 2022; published 18 January 2023)

Despite the exciting implications of the Kitaev spin Hamiltonian, finding and confirming the quantum spin-liquid state have proven incredibly difficult. Recently, the applicability of the model has been expanded through the development of a microscopic description of a spin-1 Kitaev interaction. Here we explore a candidate spin-1 honeycomb system, $KNiAsO_4$, which meets many of the proposed criteria to generate such an interaction. Bulk measurements reveal an antiferromagnetic transition at ∼19 K which is generally robust to applied magnetic fields. Neutron diffraction measurements show magnetic order with a $\mathbf{k} = (\frac{3}{2}, 0, 0)$ ordering vector which results in the well-known "zigzag" magnetic structure thought to be adjacent to the spin-liquid ground state. Field-dependent diffraction shows that while the structure is robust, the field can tune the direction of the ordered moment. Inelastic neutron scattering experiments show a well-defined gapped spin-wave spectrum with no evidence of the continuum expected for fractionalized excitations. Modeling of the spin waves shows that the extended Kitaev spin Hamiltonian is are generally necessary to model the spectra and reproduce the observed magnetic order. First-principles calculations suggest that the substitution of Pd on the Ni sublattice may strengthen the Kitaev interactions while simultaneously weakening the exchange interactions thus pushing $KNiAsO_4$ closer to the spin-liquid ground state.

DOI: 10.1103/PhysRevResearch.5.013022

I. INTRODUCTION

The Kitaev Hamiltonian for the spin-$\frac{1}{2}$ honeycomb lattice system is a rare case of an exactly solvable model that also produces exciting physics with imminently useful properties [1]. This confluence of features has driven a massive research effort into studying the phase space and properties of the model and its extensions, searching and designing materials which actually host the prescribed Kitaev interactions, and developing methods to manipulate the resultant topological physics for quantum computation [2–7]. As a result of this effort, $RuCl_3$ has emerged as a leading candidate material allowing for the observation of many of the proposed experimental properties of the Kitaev quantum spin liquid (QSL) exhibiting fractionalized excitations and fractionalized thermal transport and leading to the development of extended Kitaev Hamiltonians for real materials which have additional perturbing interactions [8–11].

Key to this discussion is the "Kitaev" interaction which describes an Ising-like interaction along each of the three metal-metal directions for any given site on the honeycomb [1]. This provides an alternate route to a quantum spin-liquid state to the well-known resonating valence state proposed by Anderson as a potential explanation for high-temperature superconductivity [12]. Such an interaction in a spin-$\frac{1}{2}$ system leads to magnetic frustration and ultimately can give rise to topological classifications, in particular, a Z_2 classification with bipartite nearly degenerate ground-state manifolds classified by their mapping to a torus [1,13,14]. Such a Z_2 QSL invokes long-range quantum entanglement which can lead to topological excitations such as the Z_2 gauge-flux "visons" and fractionalized excitations including Majorana fermions [1,14,15]. These quasiparticles may exhibit non-Abelian statistics which would allow for braiding operations along the particle worldlines and ostensibly a robust form of quantum computation [1,16].

Yet, despite the promise of these exciting physics, finding candidate materials which exhibit the pure Kitaev interaction has proven challenging [2,17–19]. Restricting the search to materials with spin-$\frac{1}{2}$ magnetic ions on honeycomb lattices is quite limiting on its own; however, to physically realize the Kitaev interaction while minimizing other interactions, an even stricter set of conditions is imposed. Such an optimization requires that the magnetic ions be in the d^5 valence and be arranged in edge-sharing octahedra with perfect 90° bond

*taddeikm@ornl.gov
†Corresponding author: sanjeewal@missouri.edu

angles, that strong spin-orbit coupling be present, and that there be a strongly insulating state [20]. Further confounding their realization, the QSL state both is highly sensitive to disorder and often has properties which are trivially emulated by disorder leading to a difficult situation with potential false leads [21–24].

Therefore expanding the phase space and loosening the restrictions on where one might look to find applications of the Kitaev model and QSL physics are of significant value. Recently, one such effort has been in extending the model to systems with spin S greater than $\frac{1}{2}$ [25]. However, for $S > \frac{1}{2}$, it is not guaranteed that a Kitaev model is realizable, that the resulting state is a QSL, or that such a QSL would host the desired excitations. The key difficulties here are that for $S > \frac{1}{2}$ the Kitaev Hamiltonian is not analytically solvable and until recently no microscopic model for contriving Kitaev interactions for such a state existed. Excitingly, this latter difficulty has been overcome by the development of a microscopic model for a spin-1 system [26]. In this model, Kitaev interactions were generated via many of the same requirements as in the spin-$\frac{1}{2}$ case requiring spin-orbit coupling, a honeycomb lattice of edge-sharing octahedrally coordinated transition metal ions, and a large Hund's coupling creating a Mott insulator state [26]. Additionally, numerous numerical approaches have been used in attempts to address the solvability issue and have suggested that the $S = 1$ case still supports a QSL state indicating a possibility for topological physics and long-range entanglement [25,27,28]. Encouragingly, in these studies both ferromagnetic (FM) and antiferromagnetic (AFM) Kitaev interactions were suggested to generate a QSL making the spin-1 model relatively permissive [26,28].

However, due to the lack of an analytical solution, the nature of the potential QSL state remains contested. Different numerical approaches have led to the emergence of conflicting predictions, with proposals of both gapped and gapless QSL ground states with a possible Z_2 topology and topological quasiparticle excitations, some of which are not found in the spin-$\frac{1}{2}$ system [27–31]. In general, predictions of nontrivial topology seem universal; yet despite the expectation for exotic quasiparticles, some analyses have reported that such a QSL may not generate Majorana fermions or non-Abelian quasiparticles as may be intuitive considering the spin [27–29,32,33]. Nevertheless, it is of great interest to find such a spin-1 Kitaev material to test these predictions and attempt to extend the phase space of QSLs and the general understanding of the Kitaev interaction and Hamiltonian.

Thus far, few candidate spin-1 honeycomb systems have been found (though there has been success in identifying $S > 1$ materials) with $Na_{2-x}Ni_2TeO_6$ perhaps being the most well studied [34–40]. This system crystallizes in the $P6_3/mcm$ space group with stacked Ni^{2+} honeycomb layers built of NiO_6 octahedra, thus indicating the potential for spin-1 Kitaev physics [37]. Recently, a comprehensive neutron scattering study on the $Na_2Ni_2TeO_6$ member found a "zigzag" magnetic ground state and a spin-wave spectrum which required the extended Kitaev Hamiltonian to model, adding to the material's promise [37]. However, disagreements between the ground-state structure and the energy-minimized structure of the spin Hamiltonian have complicated the analysis and indicated the need for more complex modeling potentially leaving this material further removed from the pure Kitaev state [37].

Another potential candidate spin-1 honeycomb compound is $KNiAsO_4$, which was first discovered and studied several decades ago as a "micalike" material with potential for organic ion exchange [41–44]. $KNiAsO_4$ crystallizes in the trigonal $R\bar{3}$ space group (in the hexagonal setting) with a layered structure of edge-sharing NiO_6 octahedra which create an expected spin-1 Ni^{2+} honeycomb sublattice [41,43]. These Ni layers are highly two dimensional (2D) with a large $\sim$10 $Å^{-1}$ interlayer spacing which should strongly suppress interlayer interactions, while the overall material has strong insulating characteristics (growing as transparent greenish-yellow crystals) [41]. Thus $KNiAsO_4$ appears a good candidate material for exhibiting spin-1 Kitaev physics.

Unfortunately, early work revealed that $KNiAsO_4$ undergoes an AFM transition at $\sim$19 K thus significantly reducing the chances of finding a QSL state in the as-grown compound [45]. Neutron diffraction experiments suggested an ordering vector of $\mathbf{k} = (\frac{1}{2}, 0, 0)$ with an AFM chain structure and early theoretical work (absent the Kitaev formulation) even traced out a potential phase diagram based on relative exchange interaction strengths [45]. This early analysis proposed a rich magnetic phase diagram with numerous potential magnetic states in close proximity including the well-known zigzag structure which is predicted to exist proximate to the QSL state [45]. Therefore it is worthwhile to reconsider this material to determine if it exhibits any evidence of Kitaev interactions; if so, how close to the QSL it might be; and how to optimize the structure and chemistry to tune the material closer to the pure spin-1 Kitaev model.

In this paper, we revisit the synthesis, structure, magnetic order, and phase diagram of $KNiAsO_4$, study the effects of an applied field on the magnetic ground state, and evaluate the potential for Kitaev physics via the experimental determination of the spin Hamiltonian. We find a ground-state magnetic structure of the zigzag type indicating the potential presence of the Kitaev interaction. Using inelastic neutron scattering, we find that the spin-wave spectrum is most consistent with an extended Kitaev Hamiltonian with both Kitaev and Heisenberg interactions. Using first-principles calculations, we consider how $KNiAsO_4$ might be chemically tuned to strengthen the Kitaev and weaken the Heisenberg interactions. These results suggest that $KNiAsO_4$ is a useful system to study Kitaev physics in a spin-1 honeycomb lattice.

II. EXPERIMENTAL METHODS

A. Synthesis

Powder samples of $KNiAsO_4$ were synthesized using a stoichiometric mixture of KH_2AsO_4 and $Ni(NO_3)_2 \cdot 6H_2O$. In a typical reaction, a total of 3 g of KH_2AsO_4 and $Ni(NO_3)_2 \cdot 6H_2O$ were mixed in a 1 : 1 stoichiometric molar ratio and ground well using an agate motor and pestle inside an inflatable glove chamber due to both KH_2AsO_4 and $Ni(NO_3)_2 \cdot 6H_2O$ being highly hygroscopic. Next, the mixture was loaded into an alumina crucible and heated to 300 °C overnight. After the initial heating, the mixture was ground and pelletized. These pellets were then reheated to 900 °C for 2 days in an Ar

atmosphere, after which a homogeneous greenish powder was obtained with powder x-ray diffraction confirming the quality and purity of the sample. Once finished, powder samples were transferred to an Ar-filled glovebox to prevent moisture absorption.

Single crystals were synthesized starting with powder samples grown as described above. Using a flux growth, the well-ground $KNiAsO_4$ powder was mixed with KCl at 1 : 10 mass ratio and sealed in evacuated quartz ampoules. The ampoules were then heated up to 900 °C at 60 °C/h and left to dwell at temperature for 7 days. After this the reaction was cooled to 400 °C at 5 °C/h and then furnace cooled to room temperature. Once at room temperature, high-quality green platelike crystals were recovered from the flux by washing with deionized water. As with the powders, the crystals were stored in the glovebox in order to prevent any reaction with air.

B. Magnetization and heat capacity experiments

Temperature- and field-dependent magnetic properties were measured in a Quantum Design (QD) Magnetic Properties Measurement System (MPMS). The temperature-dependent static susceptibility $[M/H(T)]$ was measured over a temperature range 2–300 K with applied fields between 0.1 and 5 T using single-crystal samples with the field oriented parallel and perpendicular to the **c** axis (i.e., the surface of the plates). Isothermal magnetization measurements were performed at 2 K for fields up to 6 T. Heat capacity was measured on single-crystal samples in the QD Physical Properties Measurement System (PPMS) by the relaxation technique. Measurements were performed in both $\mathbf{H}||\mathbf{c}$ and $\mathbf{H} \perp \mathbf{c}$ orientations up to 9 T; however, only $\mathbf{H} \perp c$ results are shown due to the similarity of the signals in either orientation.

C. Neutron scattering experiments

Neutron powder diffraction (NPD) measurements were performed using the constant-wavelength powder diffractometer HB-2A of Oak Ridge National Laboratory's (ORNL's) High Flux Isotope Reactor (HFIR) [46]. To prevent grain reorientation and sample movement during measurements in an applied field, the powder sample was pressed into pellets and secured in the sample can with a thin Al post. Analysis of the neutron powder diffraction data was performed using the Rietveld method as implemented in the FULLPROF software suite [47]. For the magnetic structure determination, the Simulated Annealing and Representational Analysis (SARAH) software was used as well as the Bilbao Crystallographic Server [48–51]. Visualization of the nuclear and magnetic crystal structures was performed using Visualization for Electronic and Structural Analysis (VESTA) [52].

Inelastic neutron scattering (INS) experiments were carried out on the Hybrid Spectrometer (HYSPEC) direct-geometry spectrometer of ORNL's Spallation Neutron Source [53]. Measurements were performed on powder samples, and the data shown in this paper were collected using an incident neutron energy of $E_i = 13$ meV and a Fermi chopper frequency of 300 Hz. This configuration provided an energy resolution of 0.4 meV (determined from the full width at half maximum at the elastic line). Analysis of the obtained spectra was performed using a machine-learning optimization algorithm developed by the authors and linearized spin-wave theory as implemented in SPINW [54,55].

D. First-principles calculations

First-principles calculations were performed using the linearized augmented plane-wave (LAPW) density functional theory code WIEN2K, using both the generalized gradient approximation (GGA) and the commonly used "GGA+U" approximation, in which an orbital potential U was applied to the magnetic Ni $3d$ orbitals [56–58]. To avoid attempting to fit the data using first-principles efforts, only a single U of 5 eV was used in the calculations. In general, the application of a U further localizes the relevant electrons and hence reduces the exchange energies associated with magnetic order, and we will see that this is true here.

Sufficient numbers of k points (a minimum of 600 in the relevant Brillouin zone) were used to make the ordered magnetic moments and associated energies of sufficient accuracy—generally to at least 10^{-2} μ_B and 10^{-4} eV for the in-sphere magnetic moment and total energy, respectively. The experimentally determined lattice parameters were used, and the internal coordinates were relaxed, within the "straight" GGA approach in an assumed ferromagnetic configuration, until atomic forces were less than 2 mRy/bohr. Including magnetic order in the relaxation helps to guard against the risk that the neglect of magnetoelastic effects in non-spin-polarized calculations yields a structure far from the experimental one [59–63]. Forces in the experimental antiferromagnetic state (see below) remain small. Spin-orbit coupling was not included in these calculations. LAPW sphere radii of 1.42, 1.57, 1.99, and 2.37 bohrs were used for O, As, Ni, and K, respectively, and an RK_{max} value of 7.0 was employed. This represents the product of the smallest sphere radius—in this case O—and the largest plane-wave expansion wave vector. Ordinarily for high-precision computational work a larger value (typically 9.0) is more desirable, but in this case the relatively small sphere radius applicable to O means that the effective RK_{max} applicable to the magnetically relevant Ni is in fact well in excess of 9.0, so that one may be reasonably assured of the accuracy of these calculations.

III. RESULTS AND DISCUSSION

A. Nuclear structure

Previous reports suggest that $KNiAsO_4$ crystallizes in the trigonal $R\bar{3}$ space group (hexagonal setting) in a "micalike" layered structure as is shown in Figs. 1(a)–1(c) [41,42,45,64]. Due to the trigonal symmetry, all four atom species form triangular lattices which are then shifted and stacked along the c axis by the centering operations and mirrored by the rotoinversion. In the case of the Ni site, the z position of ~0.16, which is close to $\frac{1}{2}$ of $\frac{1}{3}$, leads the layers generated by the centering operations to be nearly positioned on the same plane, creating very slightly buckled hexagonal layers of Ni. These Ni layers are then sandwiched between O layers describing a hexagonal lattice of NiO_6 octahedra. The NiO_6 lattice is capped by triangular lattices of As which cover the

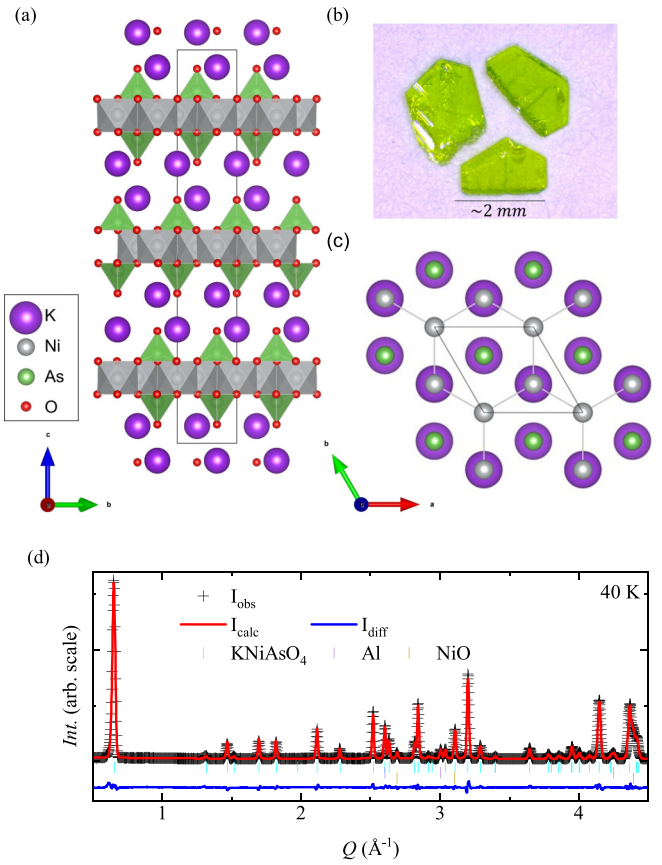

FIG. 1. (a) Crystal structure of $KNiAsO_4$ shown along the **a** axis illustrating the layered structure. (b) Picture of as-grown single crystals of $KNiAsO_4$ with the longest edge of the crystals being ~2 mm. (c) Crystal structure viewed along the **c** axis. (d) Rietveld profile of the fit to the 40-K neutron powder diffraction data. Int., intensity; arb., arbitrary.

TABLE I. Crystallographic parameters of $KNiAsO_4$ at 40 and 2 K under 0 T and at 2 K with a 6 T applied field. The magnetic moment is reported in units of μ_B/Ni.

	40 K, 0 T	2 K, 0 T	2 K, 6 T
Space group	$R\bar{3}$	$R\bar{3}$	$R\bar{3}$
R_{wp}	8.53	8.43	8.29
χ^2	17.99	16.72	3.10
a (Å)	4.9864(1)	4.9868(1)	4.9858(1)
c (Å)	28.6182(6)(2)	28.6192(6)	28.6162(5)
V (Å^3)	616.06(1)	616.37(1)	616.06(1)
K (6c)			
x	0	0	0
y	0	0	0
z	0.2893(2)	0.2893(2)	0.2893(2)
Ni (6c)			
x	0	0	0
y	0	0	0
z	0.1653(2)	0.1652(1)	0.1653(3)
m_a		−0.2(1)	−1.3(1)
m_b		1.6(1)	0.4(1)
m_c		0.7(1)	0.2(1)
$\|\mathbf{m}\|$		1.8(2)	1.5(2)
As (6c)			
x	0	0	0
y	0	0	0
z	0.5596(1)	0.5599(1)	0.5596(1)
O1 (18f)			
x	0.0050(6)	0.0060(5)	0.0050(6)
y	0.3447(5)	0.3454(4)	0.3447(5)
z	0.1255(1)	0.1249(1)	0.1255(1)
O2 (6c)			
x	0	0	0
y	0	0	0
z	0.6178(1)	0.6183(1)	0.6178(1)

center of the Ni hexagons making AsO_4 tetrahedra [Figs. 1(a) and 1(c)]. These Ni-As-O layers stack along the c axis with the interlayers filled by offset triangular lattice K sheets [41,64].

To check this structure, originally reported several decades ago, we performed NPD at temperatures above the Néel temperature T_N and modeled the resulting pattern using the $R\bar{3}$ structure [as shown in Fig. 1(d)]. In our Rietveld refinements, the $R\bar{3}$ structure satisfactorily accounted for all observed peak positions and peak intensities save for a small (~1% volume fraction) impurity phase of NiO and peaks originating from the Al sample can. During our modeling we attempted to refine the K, Ni, and O site occupancies individually; however, all sites were refined to within 1% of fully occupied. Considering the relatively low Q range of this study which is optimized to capture magnetic scattering rather than structural peaks, in the final refinements we fixed all site occupancies to fully occupied. Therefore we use this reported structure for the rest of our analysis. The lattice and atomic parameters extracted from the refinements at various temperatures are shown in Table I. Of particular interest here is the sizable **c** lattice parameter, which leads to ~10 Å of separation between the Ni layers and thus should encourage strongly two-dimensional physics.

B. Bulk magnetic properties

Previously, $KNiAsO_4$ was reported to have an AFM transition at ~19 K from magnetic susceptibility measurements; here we revisit such measurements with modern instrumentation and expand on them by measuring the field dependence [45]. In Fig. 2(a) we show the susceptibility and its inverse as functions of temperature along two different crystallographic directions (**H** ∥ **c** and **H** ⊥ **c**). Upon cooling, we first observe a broad peak at ~30 K, followed by a steep downturn at ~20 K. Such a broad peak-like feature in two-dimensional systems can be indicative of two-dimensional magnetic correlations preceding the long-range three-dimensional order [65,66]. Using heat capacity measurements [Fig. 2(b)], we observe a sharp lambda-like anomaly at ~19 K. Consequently, we label the AFM transition as occurring at ~19 K. Comparing the behavior along the different crystallographic directions (i.e., in-plane and along **c**), we find that while the in-plane signal shows a sharp downturn, along **c** a much smaller drop is observed perhaps indicating a larger moment component in the ***ab*** plane. We also observe an upturn in the **H** ∥ **c** signal below ~10 K. However, as will be discussed this is not observed in any other probe used, and so we do not attribute it to an observable change in the magnetic

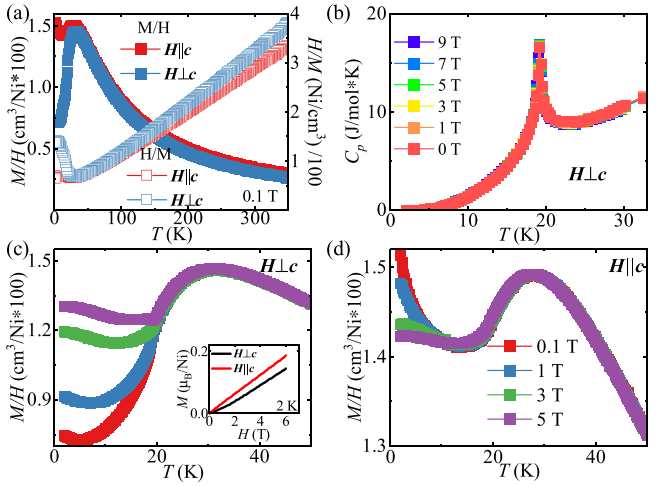

FIG. 2. (a) Magnetic susceptibility and inverse susceptibility of $KNiAsO_4$ collected parallel and perpendicular to the **c** axis for a probe field of 0.1 T. (b) Heat capacity C_p measured for $\mathbf{H} \perp \mathbf{c}$ for applied fields between 0 and 9 T (data collected for $\mathbf{H} \parallel \mathbf{c}$ are qualitatively similar and so are not shown). Temperature-dependent magnetic susceptibility collected between 2 and 50 K under applied fields between 0.1 and 5 T for (c) $\mathbf{H} \perp \mathbf{c}$ and (d) $\mathbf{H} \parallel \mathbf{c}$. The inset in (d) shows the isothermal magnetization collected along the two field orientations.

ground state at these temperatures. Such a low-temperature upturn is often seen and is usually attributed to small contaminants or impurity phases though intrinsic mechanisms are possible; such an identification is beyond the scope of this work [67–71].

Using the inverse susceptibility curves, we performed Curie-Weiss fitting to extract the effective moment μ_{eff} and the Curie-Weiss temperature θ_{CW}. We note that in this analysis a high sensitivity of the fit parameters to the fit temperature range was observed (as is common in lower-dimensional and frustrated systems), and so a high temperature range of $180 < T < 350$ K was used in the fits [45]. Doing so resulted in fit parameters of $\theta_{\text{CW}} = -0.2 \pm 0.5$ K and $\mu_{\text{eff}} = 2.7 \pm 0.1\ \mu_B$ for fits to the $\mathbf{H} \perp \mathbf{c}$ inverse susceptibility and of $\theta_{\text{CW}} = -16.1 \pm 0.4$ K and $\mu_{\text{eff}} = 2.9 \pm 0.1\ \mu_B$ for the $\mathbf{H} \parallel \mathbf{c}$ curve. Here, the μ_{eff} is close to that expected for a $S = 1$, $3d$ transition metal ion. On the other hand, while both fits produced negative θ_{CW}, suggesting AFM interactions, the temperatures are quite different. The in-plane $|\theta_{\text{CW}}|$ is significantly smaller than that of the out-of-plane value. This is unexpected given the quasi-2D layered structure. However, similarly large out-of-plane Curie-Weiss temperatures have been obtained in other quasi-2D honeycomb materials with Kitaev interactions and been ascribed to the effects of off-diagonal exchange terms (see Sec. III D) perhaps indicating some similarity here to those systems [72–74]. Alternatively, this could be interpreted more straightforwardly as $KNiAsO_4$ exhibiting much stronger out-of-plane than in-plane exchange interactions. However, while perhaps not impossible, this seems quite difficult to explain given the >9-Å interlayer separation. Whatever the cause of this seemingly inverted anisotropy, more detailed magnetic susceptibility measurements are needed both to understand this result and to uncover possible physical mechanisms behind it.

In Figs. 2(c) and 2(d) we show the low-temperature behavior of the transition at different probe fields for the two crystal orientations. For $\mathbf{H} \perp \mathbf{c}$ we find that increasing field decreases the magnitude of the signal drop after the transition. Similarly, for $\mathbf{H} \parallel \mathbf{c}$ the upturn in the curve at low temperatures decreases with increasing field perhaps indicating that the field is tuning the direction of the moment. However, in either case the T_N shows no significant change even at the highest measured field of 5 T, and no evidence of a second transition is observed suggesting only a spin reorientation in the existing magnetic symmetry but no metamagnetic transition [75,76]. As a further check, the heat capacity was measured as a function of temperature and applied field in both orientations [Fig. 2(b); $\mathbf{H} \parallel \mathbf{c}$ is not shown but looks identical to $\mathbf{H} \perp \mathbf{c}$], and while a sharp peak is observed at 0 T, it shows no field dependence; no evidence of a second transition is observed at any temperature for fields up to 9 T.

C. Magnetic structure and field dependence

With the bulk measurements indicating an AFM transition at ∼20 K we next turn to neutron powder diffraction to solve the magnetic structure. In Fig. 3(a) we show neutron powder diffraction patterns collected above and below the signal observed in the susceptibility. Upon cooling below T_N, numerous new reflections appear which cannot be indexed by the nuclear structure indicating AFM ordering. To better associate these new peaks with the signal seen in the bulk measurements, an order parameter scan was performed by collecting the intensity of the peak at ∼0.76 Å^{-1} as a function of temperature (with the intensity of a magnetic Bragg peak being proportional to the square of the ordered moment) as shown in Fig. 3(b). The peak intensity is seen to grow below 20 K consistent with the behavior observed in the susceptibility.

To solve the magnetic structure, we first identify ordering vectors which can account for the observed reflections. As shown in Fig. 3(a) all the additional low-temperature peaks can be indexed by $\mathbf{k} = (\frac{3}{2}, 0, 0)$ [we note that here $\mathbf{k} = (\frac{3}{2}, 0, 0)$ is indicated rather than $\mathbf{k} = (\frac{1}{2}, 0, 0)$ due to the observed extinction rule $-h + k + l = 3n$]. Using representational analysis, this **k** together with the $R\bar{3}$ space group and $6c$ Wyckoff position of the Ni^{2+} ion allows two possible irreducible representations (irreps Γ), each of which split the $6c$ site into two symmetry-related sites (one with the original position and one at $x, y, -z$) with a total of three basis vectors—one each for the three crystallographic directions (see Table II). Of the two Γ, the first gives rise to a "stripy"-type magnetic order with AFM along the zigzag chains in the [010] direction of the honeycomb lattice and FM correlations between the chains. The second Γ describes a "zigzag" order with FM along the chains and AFM between them. Both of these Γ correspond to the magnetic space group (MSG) $P_S\bar{1}$ with a doubling of the a lattice parameter and an origin shift of $(\frac{1}{2}, 0, 0)$ in the case of Γ_2.

Rietveld refinements were performed using both of these models, and the zigzag structure of Γ_2 was found to produce a decisively better fit to the experimental pattern. The resulting profile together with the data is shown in Fig. 3(c), and the

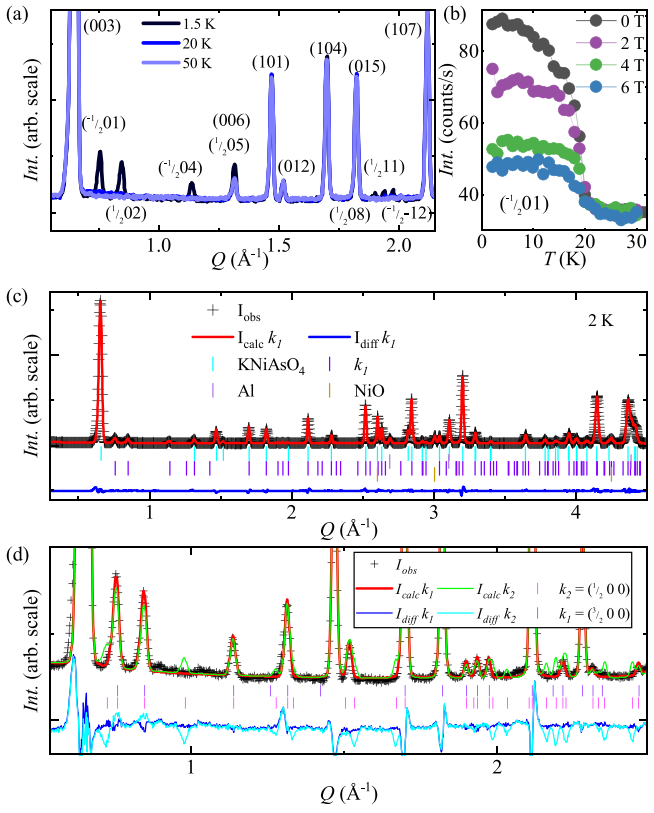

FIG. 3. (a) Comparison of powder diffraction patterns collected at 1.5, 20, and 50 K with peak indices showing the appearance of new fractional integer peaks below T_N. (b) Temperature-dependent order parameter scans for the $(-\frac{1}{2}, 0, 1)$ peak collected on warming under different applied fields. (c) Rietveld profile to the 2-K diffraction pattern for the best-fit magnetic model. (d) Rietveld profile comparison of the previously reported magnetic structure [with $\mathbf{k} = (\frac{1}{2}, 0, 0)$] and the $\mathbf{k} = (\frac{3}{2}, 0, 0)$ structure reported here.

extracted crystallographic and magnetic structure parameters are reported in Table I. The obtained magnetic structure (Fig. 4) has FM zigzag chains running along the [010] direction of the unit cell with AFM coupling to the neighboring chains (i.e., along **a**). The $P_S\bar{1}$ MSG allows the magnetic moments to have nonzero components in all three crystallographic directions, and in our refinements we found it necessary to allow all three components to be nonzero to

TABLE II. Irreducible representations Γ, basis vectors ψ, magnetic space group (MSG), magnetic supercell, and origin shift for $\mathbf{k} = (\frac{3}{2}, 0, 0)$. Basis vectors contain components for the two generated Ni sites, the original at (0,0,0.165) indicated by ψ_1 and a second at (0,0,0.835) indicated by ψ_2.

Γ	ψ_1	ψ_2	MSG	Supercell	Origin shift
Γ_1	(1,0,0)	(1,0,0)	$P_S\bar{1}$	$(2a, b, c)$	(0,0,0)
	(0,1,0)	(0,1,0)			
	(0,0,1)	(0,0,1)			
Γ_2	(1,0,0)	$(-1, 0, 0)$	$P_S\bar{1}$	$(2a, b, c)$	$(\frac{1}{2}, 0, 0)$
	(0,1,0)	$(0, -1, 0)$			
	(0,0,1)	$(0, 0, -1)$			

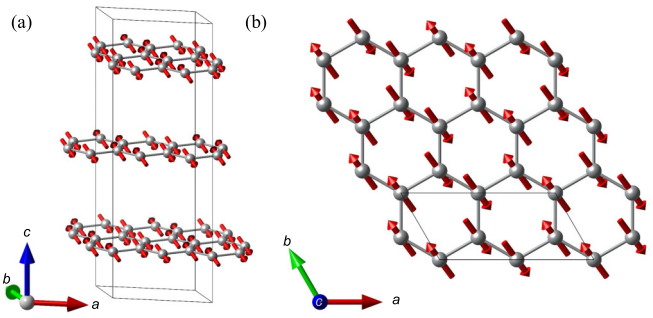

FIG. 4. Best-fit magnetic structure of $KNiAsO_4$ oriented to visualize (a) the stacking relationship of the Ni planes along the **c** direction and (b) the magnetic order in a single Ni layer.

obtain the best fit. In the refined structure, the majority of the moment lies in the **ab** plane with a small component along **c** describing an ∼22° canting (see Table II). The magnitude of the ordered moment is 1.8(2) μ_B/Ni, which is smaller than the effective moment but very close to the expected size for a spin-1 system [45,64].

We note that the magnetic structure found here is different from that reported in Ref. [64], and so it is worth considering this previous model more carefully. In Ref. [64] a $\mathbf{k} = (\frac{1}{2}, 0, 0)$ was suggested with a magnetic structure that doubled the cell along **a** (or **b**) and re-created a stripy-type structure. In our analysis using representational analysis, $\mathbf{k} = (\frac{1}{2}, 0, 0)$ breaks the 6*c* Wyckoff site into two separate orbits (or symmetry-distinct atomic sites) with the same positions as described for the symmetry-related atoms in the $\mathbf{k} = (\frac{3}{2}, 0, 0)$ structures and produces only a single Γ for either orbit. This Γ has three basis vectors per site—one for each crystallographic direction leading to a total of six parameters and allowing the two sites to have differently sized ordered moments. Using this model, we again performed Rietveld refinements, and the best fit is shown in Fig. 3(d) together with the fit from the $\mathbf{k} = (\frac{3}{2}, 0, 0)$. Here it is clear that the $\mathbf{k} = (\frac{3}{2}, 0, 0)$ zigzag model accounts for both the observed peak positions and intensities better than the $\mathbf{k} = (\frac{1}{2}, 0, 0)$ model with the latter adding magnetic peaks where no new intensity is seen while also not correctly fitting the observed intensities. We suggest that this discrepancy with the previous report likely results from our use of a higher-intensity, higher-resolution instrument, which allowed us to observe many more magnetic peaks than in the previous work as well as the development of more powerful tools for magnetic structure solution in the intervening time. Therefore we continue our analysis using our zigzag magnetic structure.

Having established the zigzag structure as the zero-field magnetic ground state, we turn to the field-dependent structure. Shown in Fig. 5(a) are several powder patterns collected under different applied fields together with the 0-T, 1.5-K data and the 0-T, 40-K data for comparison. Focusing on the most intense low-angle peaks [the $(-\frac{1}{2}, 0, 1)$ and $(\frac{1}{2}, 0, 2)$ reflections], we see that as the field is increased the magnetic intensity monotonically decreases to the highest measured field of 6 T [Fig. 5(c)]. However, the reduction in intensity is not identical between the peaks with the $(-\frac{1}{2}, 0, 1)$ changing from the more intense peak at 0 T to the weaker reflection

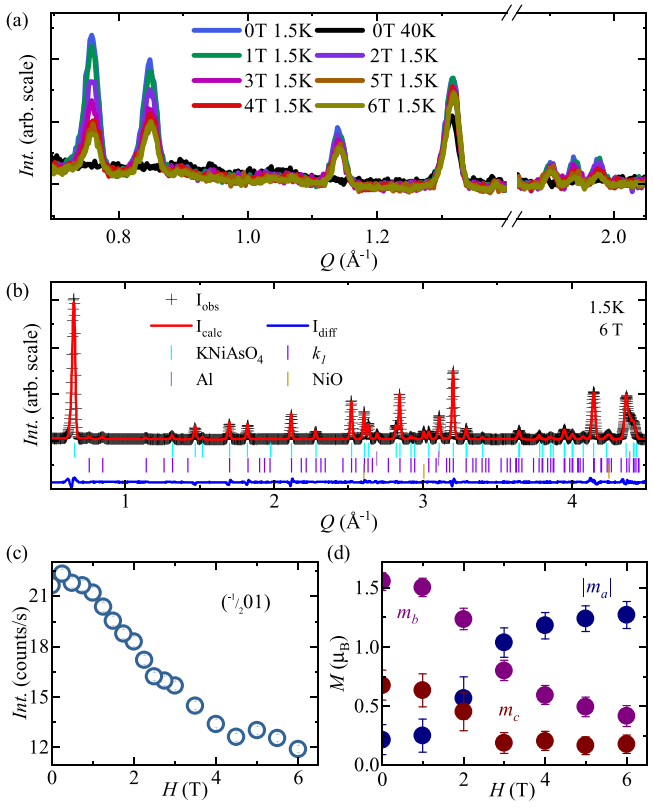

FIG. 5. (a) Powder diffraction patterns under different applied fields. (b) Rietveld profile fit of data collected at 1.5 K under a 6 T applied field using the magnetic structure determined from the analysis of the 0-T data. (c) Order parameter scan collected upon warming from 1.5 K on the $(-\frac{1}{2}, 0, 1)$ magnetic peak. (d) Refined components of the Ni^{2+} magnetic moment as a function of applied field.

by 6 T. Similarly, considering the three reflections between 1.9 and 2 $Å^{-1}$, we see the intensity of the two higher-angle peaks decreases with increasing field while the lower-angle peak remains nearly constant. These observations imply that the increasing field has two effects on the magnetic structure, reducing the ordered moment and changing its direction with respect to the nuclear structure, both of which are broadly consistent with the magnetization data previously discussed. This is further supported by considering the temperature dependence of the $(-\frac{1}{2}, 0, 1)$ peak under different applied fields [Fig. 3(b)] and at 2 K as a function of field [Fig. 5(c)]. In the former, as in the heat capacity measurements, we see no change in the transition temperature. In the latter we see a continuous decrease in intensity to the highest measured field. In either case, no sign of a phase transition is observed.

Ideally, one would like to extract the behavior of the magnetic field along different crystallographic directions; however, in this paper, such measurements were not feasible. Therefore, despite the orientational averaging of the powder data, we nevertheless performed quantitative analysis by modeling the magnetic scattering observed in the data collected under an applied field. We note that since no metamagnetic transition was observed, which in such measurements can lead to multiple macroscopically coexisting magnetic structures due to the different field orientations of different powder grains (see, for instance, Ref. [77]), analysis of the field-dependent data may just give additional insights into which crystallographic directions are more magnetically soft.

In Fig. 5(b) we show a fit using the zigzag model of the data collected at 1.5 K and 6 T. As seen, despite the discussed difficulties, the calculated intensities match the experimental profile remarkably well without the need for additional magnetic phases to account for different relative field orientations, with similar quality fits obtained for all measured fields. To elucidate the above-described field dependence, we extracted the independent components of the refined magnetic moment [Fig. 5(d)]. As the field is increased, we find a monotonic decrease in the magnitude of both m_b and m_c while the magnitude of m_a increases thus describing a rotation of the moments to be more in-plane and more perpendicular to the chain direction. We note that in our refinements we also found the field to drive a slight contraction of both the a and c lattice parameters, which both continuously decrease with increasing field.

Finding the zigzag order in $KNiAsO_4$ is quite interesting. In both the spin-$\frac{1}{2}$ and spin-1 Kitaev models on a honeycomb lattice, the zigzag magnetic ground state is expected to be adjacent to the Kitaev state [28,78,79]. In calculations, the zigzag structure is found to stabilize from a spin Hamiltonian which contains both Kitaev and Heisenberg interactions [78]. Thus perhaps the observed structure is evidence of a proximity to Kitaev physics in $KNiAsO_4$, a case we consider more rigorously in the next section.

D. Spin waves and the spin Hamiltonian

While the realized long-range order allows us to place $KNiAsO_4$ on established generic phase diagrams of the perturbed Kitaev Hamiltonian, to better elucidate whether it actually exhibits Kitaev interactions, it is necessary to study the spin dynamics of the system. Shown in Fig. 6(a) is the INS spectrum for a powder sample of $KNiAsO_4$ collected at 2 K using the HYSPEC spectrometer with an incident energy of $E_i = 13$ meV. Here, we see well-defined excitations with several acoustic modes arising from approximately 0.75, 2, and 2.6 $Å^{-1}$ and optical modes around 4.5 and 7 meV as expected for an AFM structure. At low energies the acoustic modes are seen to have an energy gap of $\sim$1 meV indicating some explicit symmetry breaking in the underlying spin Hamiltonian.

Such behavior is unlike that of the canonical proximate QSL α-$RuCl_3$, where even powder INS evidenced heavily damped, broad excitations indicative of the QSL state, though it is worth noting that in the spin-1 QSL such fractionalized excitations may not be expected in the spin channel [8,32]. Rather, here the spectrum looks well ordered as seen recently in other Kitaev candidate materials such as $Na_2Co_2TeO_6$, $Na_2Ni_2TeO_6$, $BaCo_2(AsO_4)_2$, and Na_2IrO_3 [37,80,81]. Nevertheless, it is important to determine whether the found ordered state results from Kitaev interactions to understand if and how one could tune the interactions towards a Kitaev state.

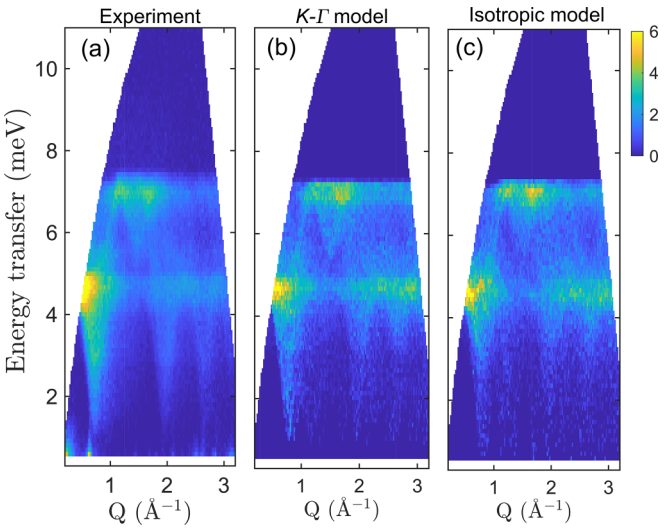

FIG. 6. (a) Powder inelastic neutron spectrum $[S(q, \Delta E)]$ of $KNiAsO_4$ measured on HYSPEC using $E_i = 15$ meV at 2 K. Calculated INS spectra from best-fit parameters for the (b) Γ-K and (c) ISO spin Hamiltonians.

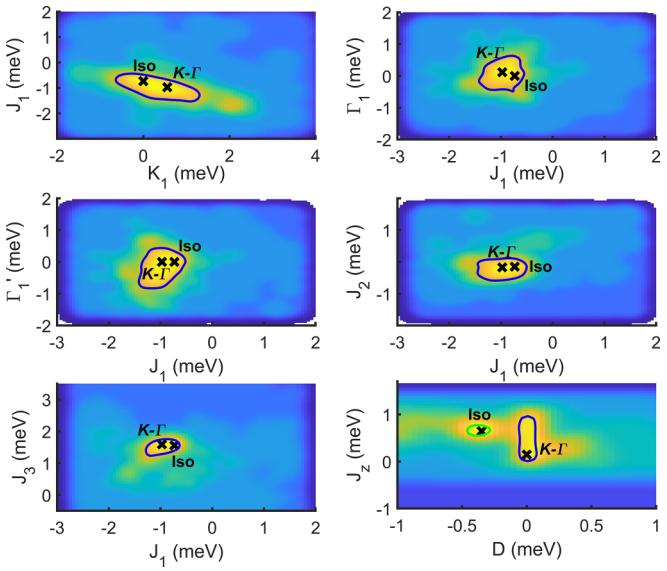

FIG. 7. Two-dimensional cuts of the higher-dimensional spin-Hamiltonian optimization manifold with the color scale indicating the χ^2 of the given parameter's modeling of the observed spectra. Small and large values of $\hat{\chi}^2_{\rm INS}$ are indicated by yellow and blue, respectively, on a logarithmic scale.

To explicate the spin Hamiltonian, linear spin-wave theory (as implemented in SPINW) was used to fit the observed spectra with several different trial Hamiltonians. Of these, here we focus on the extended Kitaev (Γ-K) and the isotropic (ISO) Heisenberg models as they provided the best fits of the observed spectra (we note that an XXZ model produced similar quality fits to the ISO model but with less reasonable parameters) [20,37,82]. A generalized form of the spin Hamiltonian is shown in Eq. (1).

$$\begin{aligned}\mathcal{H}_{\Gamma\text{-}K} = &\sum_{\langle ij\rangle} J\vec{S}_i\cdot\vec{S}_j + \sum_{\langle ij\rangle}\left[KS_i^\gamma S_j^\gamma + \Gamma\left(S_i^\alpha S_j^\beta + S_i^\beta S_j^\alpha\right)\right.\\ &\left.+\Gamma'\left(S_i^\alpha S_j^\gamma + S_i^\gamma S_j^\alpha + S_i^\beta S_j^\gamma + S_i^\gamma S_j^\beta\right)\right]\\ &- D\sum_i (S_i\cdot\tilde{n}_i)^2. \end{aligned} \quad (1)$$

In Eq. (1), the indices $\langle ij\rangle$ run over first, second, and third in-plane nearest-neighbor (NN) interactions and a single interlayer interaction with associated exchange interactions of J_1, J_2, J_3, and J_z, respectively, in the first sum and over only NN interactions in the second sum. The α, β, and γ label the three Kitaev spin directions, and the K, Γ, Γ′, D, and $\tilde{n}_i$ denote the Kitaev, symmetric off-diagonal exchange, asymmetric off-diagonal exchange, single-ion anisotropy (SIA), and the SIA direction, respectively. The D term is added for generality and is only nonzero when $K \to 0$, where $H_{\Gamma\text{-}K}$ reduces to the Heisenberg XXZ-like model which can be further reduced to the ISO model by setting the off-diagonal terms (Γ and Γ′) to zero. To apply such a highly parametrized model (with a maximum of seven parameters), we used an iterative machine-learning optimization procedure together with SPINW as explained in Ref. [54] and further discussed in Ref. [37]. Figure 7 shows select slices of the resulting manifold of possible solutions plotted as contours of the cost estimator $\hat{\chi}^2_{\rm INS}$ function (which is determined from the cost function $\chi^2 = \sum_\omega \sum_Q [I_{\rm expt}(Q,\omega) - I_{\rm calc}(Q,\omega)]^2$ using the process described in Ref. [37]). Using this cost estimator, the best solutions modeling the observed INS spectra were chosen at $\hat{\chi}^2_{\rm INS}$ minima (indicated by the yellow regions in Fig. 7) and are labeled as ISO and Γ-K.

Figures 6(b) and 6(c) show the resulting simulated INS spectra calculated from the best-fit models of both the extended Kitaev and the ISO Hamiltonians (i.e., $D = 0$ and $K, \Gamma, \Gamma' = 0$, respectively) with the refined parameters shown in Table III. Surprisingly, both models are able to reproduce fairly well most of the observed scattering despite having very different physical origins—possibly due to the information lost during the powder averaging of the INS spectra. Both models reproduce the flat optical modes at ∼7.5 and ∼4.5 meV and capture the observed dispersions for the acoustic modes. Similarly, both models re-create the observed peak intensities near $(q, \Delta E) = (0.5$ Å^{-1}, 4.5 meV) and in the high-energy optic mode. However, at lower energies, Γ-K is better able to account for the observed gap at $Q \sim 0.8$ Å^{-1}, though we note that both models do produce gaps at this Q. More significantly, the ISO model requires a SIA which either underestimates or grossly overestimates the gap and is found to produce a magnetic structure with Ni^{2+} moments

TABLE III. Parameters obtained from the extended Kitaev Hamiltonian optimized to reproduce the observed spin-wave spectra. For the Γ-K model the D term is fixed to zero, while for the ISO model the K and Γ terms are fixed to zero. In the K-Γ model the Γ′ term was found unnecessary and so set to zero in the final optimization. All values are in meV.

Model	J_1	K_1	Γ_1	Γ_1'	J_2	J_3	J_z	D
K-Γ	−0.97	0.56	0.11	0	−0.17	1.6	0.15	0
ISO	−0.73	0	0	0	−0.15	1.55	0.65	−0.35

purely in the ***ab*** plane. Such features are inconsistent both with the structure found in the NPD analysis missing the moment canting and with the observed gap in the INS spectra. On the other hand, the extended Kitaev model naturally allows for the observed canted structure and accurately re-creates the experimental gap, thus indicating its potential applicability for this system.

Considering the obtained parameters, we find that the Kitaev model produces AFM Kitaev interactions with FM J_1 and J_2 exchange interactions and AFM J_3 and interlayer J_z interactions. Here J_1 and J_3 interactions are dominant with the Kitaev term being roughly half that of the J_1. This indicates that even in the extended Kitaev model the Kitaev term is not the leading interaction unlike other candidate compounds [8,37]. For the ISO model, we obtain qualitatively similar values for the exchange interactions albeit with a large increase in the interlayer interaction J_z, which surprisingly becomes similar in size to the J_1 exchange. In both models we find $|J_3| > |J_1| > |J_2|$, which is also somewhat surprising: With distances of 5.76, 2.88, and 4.988 Å, respectively, to first order, one might expect the interactions to weaken as the distance is increased. However, similar relatively strong J_3's have been reported in other honeycomb and QSL candidate systems (especially for the case of $J_3 > J_2$) and are usually found necessary to stabilize the zigzag order [37,83–85]. We note that interactions through pnictide complexes are known to at times have unintuitive behaviors suggesting the need for further single-crystal work and more thorough theoretical treatments to confirm and understand the mechanism behind this result [86].

Interestingly, the zigzag structure found in our diffraction analysis was predicted to arise in a spin-1 extended Kitaev model for $J/K < 0$ [26,27]. This is consistent with the J/K determined in our spin-wave fit using the Γ-K Hamiltonian further indicating consistency with this model. For the ISO model, the large $J_z/J_{1,2,3}$ ratio is unexpected. For similar layered transition metal honeycomb lattices the interlayer exchange interactions are typically an order of magnitude smaller than the NN exchange [37,80,81,87,88]. For $KNiAsO_4$, the inter-Ni-layer distance is $\sim$10 $Å^{-1}$, and a superexchange pathway would entail electron exchange through both the As and K layers; that such a large J_z would result is surprising and unlikely lending support to the extended Kitaev model. We note that it has been reported that buckling of the honeycomb layer can increase the out-of-plane coupling [89]. As discussed in Sec. III A, the Ni sublattice in $KNiAsO_4$ is slightly buckled, and so it is worth considering whether this could give rise to a large J_z. However, in previous work studying the effects of such buckling (e.g., Ref. [89]), while a large buckling (as measured by the displacement along **c** between sites in a single honeycomb layer) such as $\sim$0.6 Å (as observed int $CaTiO_3$) was found to enhance J_z, the effect was significantly reduced for smaller bucklings [such as the 0.16-Å displacement observed in $BaCo_2(AsO_4)_2$]. In $KNiAsO_4$ the displacement is even smaller at $\sim$0.07 Å, and so we believe it unlikely that buckling could explain the large J_z of the ISO model. Considering the slightly better visual agreement of the Γ-K model, its consistency with the observed magnetic structure, and its more physically reasonable exchange parameters, we tentatively suggest it as the more appropriate model for this system. However, additional INS studies using single-crystal samples are needed to more firmly discriminate between these models.

E. First-principles analysis of the magnetic structures

First-principles calculations were carried out to further elucidate the microscopic origins of the zigzag magnetic structure. Using density functional theory (DFT), three magnetic states were studied: A non-spin-polarized state [nonmagnetic (NM)], the FM state, and a nearest-neighbor antiferromagnetic state (AFM1) which approximates the neutron-scattering-observed ground state. We have not attempted to estimate the interlayer coupling but expect it to be quite small in view of the large Ni-Ni distances involved. However, we note that in recent work (Refs. [90,91]) even nearly negligible interlayer couplings were found sufficient to stabilize magnetic order with appreciable ordering points of order 10 K or higher, as is possibly the case here.

As expected for an oxide, even within the straight GGA the magnetic order is local in nature and falls well below the NM state in energy, with the FM state falling, within the GGA, over 800 meV/Ni below the NM state and with the AFM1 ground state some 12.9 meV/Ni below the FM state indicating the robustness of the AFM1 state. Within the GGA+U this latter energy difference is reduced to some 3.3 meV/Ni. Consistent with the expected +2 charge state and the $3d^8$ electronic configuration of Ni, we find a moment of 2 μ_B per Ni, i.e., the total cell moment is 2.00 μ_B for the FM state, with the in-sphere moment, as expected, being slightly smaller at 1.59 μ_B/Ni in the GGA and 1.74 in the GGA+U. The corresponding moments for the AFM1 state are 1.58 (GGA) and 1.74 (GGA+U); the relative insensitivity of the in-sphere magnetic moment to magnetic configuration is characteristic of local moment magnetism and in good agreement with the value determined from the Rietveld modeling [of 1.8(1) μ_B]. The AFM1 ground state is insulating, with band gaps of 1.71 eV within the GGA and 3.07 within the GGA+U.

The observed energetics would indicate estimated magnetic ordering points between 12.6 K (GGA+U) and 50 K (GGA), with the observed ordering point of 19 K bracketed by these values [62,92–94]. That the lower GGA+U value is significantly closer to the experimental value is a fair suggestion that the GGA+U-depicted localization of Ni orbitals is active here. Direct linear interpolation of the band-gap values based on the Néel point prediction suggests that the experimental band gap is likely close to 3 eV.

Next we consider via first principles how to push $KNiAsO_4$ closer to the Kitaev model. In this model the previously discussed ratio J/K plays a key role. In the true Kitaev limit, J/K approaches zero, and so in an attempt to discover Kitaev physics here we have briefly explored substitutions designed to increase K and potentially decrease J. For this purpose we have substituted, in separate calculations, one of the two in-cell Ni by the isoelectronic Pd and one of the As by the similarly isoelectronic Sb. As heavier elements, both substitutions would be expected to increase spin-orbit coupling and thus potentially the K interaction, and the generally weaker magnetic coupling of elements such as Pd would be expected

to also decrease J. For Sb alloying, the calculation immediately crashes, suggesting that the much greater volume of Sb may impede its substitution for As. For the Pd case, however, something interesting happens. Despite the calculation's initialization with the Pd moment oriented opposite to Ni, the Pd moment rapidly "flips" to become ferromagnetically coupled to the Ni and converges to a ferromagnetic solution with the same moment (4 μ_B/cell) as in the pure-Ni FM case. This inability to stabilize non-ground-state magnetic structures may indicate that Pd substitution can be expected to move the system towards itinerant behavior, with all the potential complexities associated with itinerant physics [95]. Therefore Pd substitution may drive the system towards quantum-critical behavior by frustrating the normally antiferromagnetic Ni-Ni nearest-neighbor interaction and thereby driving the ordering point towards $T = 0$. However, given that this requires doping into the honeycomb layers, it may also induce disorder and as a result lead to other more trivial yet obscuring effects. We leave this observation for future experimental efforts to exploit.

IV. CONCLUSIONS

We report the synthesis and comprehensive magnetic analysis of the spin-1 honeycomb compound $KNiAsO_4$. Crystallizing with the $R\bar{3}$ space group symmetry, $KNiAsO_4$ presents a nearly perfect layered honeycomb material with a nearly planar Ni honeycomb and a large $\sim$10 Å^{-1} interlayer spacing. Charge counting suggests a Ni^{2+} state with a $5d^8$ valence giving rise to a spin-1 system. The octahedral NiO_6 environment has nearly perfect 90° Ni-O-Ni bond angles which together with the other chemical and structural components set the stage to realize the highly desired Kitaev interaction. Magnetization and heat capacity measurements reveal an AFM transition at $\sim$19 K which is generally robust to applied magnetic fields up to 9 T. Neutron diffraction experiments as a function of temperature and field allowed for the solution of the magnetic structure revising previous reports and suggesting a $\mathbf{k} = (\frac{3}{2}, 0, 0)$ ordering vector with the ostensibly QSL proximate "zigzag" magnetic order and a refined moment of 1.8(2) μ_B—consistent with the charge counting for a spin-1 Ni valence. Neutron powder diffraction up to 6 T showed no evidence of a metamagnetic transition but did reveal that the moment direction could be tuned within the $P_S\bar{1}$ magnetic space group indicating the possibility for tuning to a **c** or **b**(**a**) polarized state in single crystals.

Using inelastic neutron scattering, the spin Hamiltonian was studied. We found that both the extended Kitaev and isotropic Heisenberg Hamiltonians were able to produce adequate simulations of the observed spectra. However, the predictions of the zigzag structure for a spin-1 Kitaev system with $J/K < 0$, the better capture of the spin gap of the Γ-K model, the inconsistent magnetic ground state of the ISO model, and its unusually large interlayer exchange all intimate a preference for the extended Kitaev Hamiltonian though additional inelastic measurements on coaligned single-crystal arrays are necessary to firmly discriminate between these models. Using first-principles calculations, we showed that the zigzag model is indeed the expected lowest-energy magnetic order and that the inclusion of a U term was important to capture the experimental T_N suggesting a highly localized system. Finally, looking to decrease the J/K ratio, we suggest alloying Pd on the Ni site, which will both increase the spin-orbit coupling, thus strengthening the Kitaev interaction, and reduce the J due to enhancing the itinerancy giving a road map to push $KNiAsO_4$ closer to the Kitaev state. Our work presents a rare example of a spin-1 honeycomb system which generally shows the possibility of proximity to a Kitaev state thus allowing for study of the associated physics in a higher-spin model than the canonical spin-$\frac{1}{2}$ quantum spin liquid.

The Department of Energy will provide public access to these results of federally sponsored research in accordance with the DOE Public Access Plan [96].

ACKNOWLEDGMENTS

The part of the research conducted at the High Flux Isotope Reactor and Spallation Neutron Source of Oak Ridge National Laboratory was sponsored by the Scientific User Facilities Division, Office of Basic Energy Sciences (BES), U.S. Department of Energy (DOE). The research is supported by the U.S. DOE, BES, Materials Science and Engineering Division. This research used resources at the Missouri University Research Reactor (MURR). This work was supported in part by a University of Missouri Research Council grant (Grant No. URC-22-021). This work has been partially supported by U.S. DOE Grant No. DE-FG02-13ER41967. ORNL is managed by UT-Battelle, LLC, under Contract No. DE-AC05-00OR22725 with the U.S. Department of Energy. The U.S. Government retains and the publisher, by accepting the article for publication, acknowledges that the U.S. Government retains a nonexclusive, paid-up, irrevocable, worldwide license to publish or reproduce the published form of this manuscript, or allow others to do so, for U.S. Government purposes.

[1] A. Kitaev, Anyons in an exactly solved model and beyond, Ann. Phys. (Amsterdam) **321**, 2 (2006).

[2] L. Savary and L. Balents, Quantum spin liquids: A review, Rep. Prog. Phys. **80**, 016502 (2017).

[3] J. R. Chamorro, T. M. McQueen, and T. T. Tran, Chemistry of quantum spin liquids, Chem. Rev. **121**, 2898 (2021).

[4] S. Trebst and C. Hickey, Kitaev materials, Phys. Rep. **950**, 1 (2022).

[5] C. Broholm, R. Cava, S. Kivelson, D. Nocera, M. Norman, and T. Senthil, Quantum spin liquids, Science **367**, eaay0668 (2020).

[6] G. Semeghini, H. Levine, A. Keesling, S. Ebadi, T. T. Wang, D. Bluvstein, R. Verresen, H. Pichler, M. Kalinowski, R. Samajdar, A. Omran, S. Sachdev, A. Vishwanath, M. Greiner, V. Vuletić, and M. D. Lukin, Probing topological spin liquids on a programmable quantum simulator, Science **374**, 1242 (2021).

[7] H. Takagi, T. Takayama, G. Jackeli, G. Khaliullin, and S. E. Nagler, Concept and realization of Kitaev quantum spin liquids, Nat. Rev. Phys. **1**, 264 (2019).

[8] A. Banerjee, C. Bridges, J.-Q. Yan, A. Aczel, L. Li, M. Stone, G. Granroth, M. Lumsden, Y. Yiu, J. Knolle, S. Bhattacharjee, D. L. Kovrizhin, R. Moessner, D. A. Tennant, D. G. Mandrus, and S. E. Nagler, Proximate Kitaev quantum spin liquid behaviour in a honeycomb magnet, Nat. Mater. **15**, 733 (2016).

[9] A. Banerjee, J. Yan, J. Knolle, C. A. Bridges, M. B. Stone, M. D. Lumsden, D. G. Mandrus, D. A. Tennant, R. Moessner, and S. E. Nagler, Neutron scattering in the proximate quantum spin liquid α-$RuCl_3$, Science **356**, 1055 (2017).

[10] T. Yokoi, S. Ma, Y. Kasahara, S. Kasahara, T. Shibauchi, N. Kurita, H. Tanaka, J. Nasu, Y. Motome, C. Hickey, S. Trebst, and Y. Matsuda, Half-integer quantized anomalous thermal Hall effect in the Kitaev material candidate α-$RuCl_3$, Science **373**, 568 (2021).

[11] J. Bruin, R. Claus, Y. Matsumoto, N. Kurita, H. Tanaka, and H. Takagi, Robustness of the thermal Hall effect close to half-quantization in α-$RuCl_3$, Nat. Phys. **18**, 401 (2022).

[12] P. Anderson, The resonating valence bond state in La_2CuO_4 and superconductivity, Science **235**, 1196 (1987).

[13] X.-G. Wen, Quantum orders and symmetric spin liquids, Phys. Rev. B **65**, 165113 (2002).

[14] *Topological Aspects of Condensed Matter Physics: École de Physique Des Houches, Session CIII, 4–29 August 2014*, edited by C. Chamon, M. O. Goerbig, R. Moessner, and L. F. Cugliandolo (Oxford University Press, Oxford, 2017).

[15] T. Senthil, S. Sachdev, and M. Vojta, Fractionalized Fermi Liquids, Phys. Rev. Lett. **90**, 216403 (2003).

[16] A. Y. Kitaev, Fault-tolerant quantum computation by anyons, Ann. Phys. (Amsterdam) **303**, 2 (2003).

[17] J. Wen, S.-L. Yu, S. Li, W. Yu, and J.-X. Li, Experimental identification of quantum spin liquids, npj Quantum Mater. **4**, 12 (2019).

[18] L. Clark and A. H. Abdeldaim, Quantum spin liquids from a materials perspective, Annu. Rev. Mater. Res. **51**, 495 (2021).

[19] J. Knolle and R. Moessner, A field guide to spin liquids, Annu. Rev. Condens. Matter Phys. **10**, 451 (2019).

[20] G. Jackeli and G. Khaliullin, Mott Insulators in the Strong Spin-Orbit Coupling Limit: From Heisenberg to a Quantum Compass and Kitaev Models, Phys. Rev. Lett. **102**, 017205 (2009).

[21] X. Rao, G. Hussain, Q. Huang, W. Chu, N. Li, X. Zhao, Z. Dun, E. Choi, T. Asaba, L. Chen, L. Li, X. Y. Yue, N. N. Wang, J.-G. Cheng, Y. H. Gao, Y. Shen, J. Zhao, G. Chen, H. D. Zhou, and X. F. Sun, Survival of itinerant excitations and quantum spin state transitions in $YbMgGaO_4$ with chemical disorder, Nat. Commun. **12**, 4949 (2021).

[22] Y. Y. Huang, Y. Xu, L. Wang, C. C. Zhao, C. P. Tu, J. M. Ni, L. S. Wang, B. L. Pan, Y. Fu, Z. Hao, C. Liu, J.-W. Mei, and S. Y. Li, Heat Transport in Herbertsmithite: Can a Quantum Spin Liquid Survive Disorder?, Phys. Rev. Lett. **127**, 267202 (2021).

[23] Z. Zhu, P. A. Maksimov, S. R. White, and A. L. Chernyshev, Disorder-Induced Mimicry of a Spin Liquid in $YbMgGaO_4$, Phys. Rev. Lett. **119**, 157201 (2017).

[24] Z. Ma, Z.-Y. Dong, S. Wu, Y. Zhu, S. Bao, Z. Cai, W. Wang, Y. Shangguan, J. Wang, K. Ran, D. Yu, G. Deng, R. A. Mole, H.-F. Li, S.-L. Yu, J.-X. Li, and J. Wen, Disorder-induced spin-liquid-like behavior in kagome-lattice compounds, Phys. Rev. B **102**, 224415 (2020).

[25] G. Baskaran, D. Sen, and R. Shankar, Spin-S Kitaev model: Classical ground states, order from disorder, and exact correlation functions, Phys. Rev. B **78**, 115116 (2008).

[26] P. P. Stavropoulos, D. Pereira, and H.-Y. Kee, Microscopic Mechanism for a Higher-Spin Kitaev Model, Phys. Rev. Lett. **123**, 037203 (2019).

[27] I. Khait, P. P. Stavropoulos, H.-Y. Kee, and Y. B. Kim, Characterizing spin-one Kitaev quantum spin liquids, Phys. Rev. Res. **3**, 013160 (2021).

[28] X.-Y. Dong and D. N. Sheng, Spin-1 Kitaev-Heisenberg model on a honeycomb lattice, Phys. Rev. B **102**, 121102(R) (2020).

[29] H.-Y. Lee, N. Kawashima, and Y. B. Kim, Tensor network wave function of $S = 1$ Kitaev spin liquids, Phys. Rev. Res. **2**, 033318 (2020).

[30] A. Koga, H. Tomishige, and J. Nasu, Ground-state and thermodynamic properties of an $S = 1$ Kitaev model, J. Phys. Soc. Jpn. **87**, 063703 (2018).

[31] A. Koga, T. Minakawa, Y. Murakami, and J. Nasu, Spin transport in the quantum spin liquid state in the $S = 1$ Kitaev model: Role of the fractionalized quasiparticles, J. Phys. Soc. Jpn. **89**, 033701 (2020).

[32] Y.-H. Chen, J. Genzor, Y. B. Kim, and Y.-J. Kao, Excitation spectrum of spin-1 Kitaev spin liquids, Phys. Rev. B **105**, L060403 (2022).

[33] Z. Zhu, Z.-Y. Weng, and D. N. Sheng, Magnetic field induced spin liquids in $S = 1$ Kitaev honeycomb model, Phys. Rev. Res. **2**, 022047(R) (2020).

[34] D. I. Badrtdinov, L. Ding, C. Ritter, J. Hembacher, N. Ahmed, Y. Skourski, and A. A. Tsirlin, MoP_3SiO_{11}: A $4d^3$ honeycomb antiferromagnet with disconnected octahedra, Phys. Rev. B **104**, 094428 (2021).

[35] Z. Zhou, K. Chen, Q. Luo, H.-G. Luo, and J. Zhao, Strain-induced phase diagram of the $S = \frac{3}{2}$ Kitaev material $CrSiTe_3$, Phys. Rev. B **104**, 214425 (2021).

[36] L. Chen, J.-H. Chung, M. B. Stone, A. I. Kolesnikov, B. Winn, V. O. Garlea, D. L. Abernathy, B. Gao, M. Augustin, E. J. G. Santos, and P. Dai, Magnetic Field Effect on Topological Spin Excitations in CrI_3, Phys. Rev. X **11**, 031047 (2021).

[37] A. M. Samarakoon, Q. Chen, H. Zhou, and V. O. Garlea, Static and dynamic magnetic properties of honeycomb lattice antiferromagnets $Na_2M_2TeO_6$, M = Co and Ni, Phys. Rev. B **104**, 184415 (2021).

[38] A. K. Bera, S. M. Yusuf, L. Keller, F. Yokaichiya, and J. R. Stewart, Magnetism of two-dimensional honeycomb layered $Na_2Ni_2TeO_6$ driven by intermediate Na-layer crystal structure, Phys. Rev. B **105**, 014410 (2022).

[39] E. Lefrançois, M. Songvilay, J. Robert, G. Nataf, E. Jordan, L. Chaix, C. V. Colin, P. Lejay, A. Hadj-Azzem, R. Ballou, and V. Simonet, Magnetic properties of the honeycomb oxide $Na_2Co_2TeO_6$, Phys. Rev. B **94**, 214416 (2016).

[40] A. I. Kurbakov, A. N. Korshunov, S. Y. Podchezertsev, M. I. Stratan, G. V. Raganyan, and E. A. Zvereva, Long-range and short-range ordering in 2D honeycomb-lattice magnet $Na_2Ni_2TeO_6$, J. Alloys Compd. **820**, 153354 (2020).

[41] G. Ladwig and B. Ziemer, Über das glimmerartige Kalium-nickel (II)-monoarsenat $KNiAsO_4$, Z. Anorg. Allg. Chem. **457**, 143 (1979).

[42] A. Buckley, S. Bramwell, D. Visser, and P. Day, Ion-exchange reactions and physical properties of the mica analogue $KNiAsO_4$, J. Solid State Chem. **69**, 240 (1987).

[43] A. Buckley, S. Bramwell, P. Day, and W. Harrison, The crystal structure of potassium nickel arsenate; $KNiAsO_4$, Z. Naturforsch. B: J. Chem. Sci. **43**, 1053 (1988).

[44] K. Beneke and G. Lagaly, The brittle mica-like $KNiAsO_4$ and its organic derivatives, Clay Miner. **17**, 175 (1982).

[45] S. Bramwell, A. Buckley, D. Visser, and P. Day, Magnetic susceptibility study of $KNiAsO_4$, $HMnAsO_4 \cdot H_2O$ and their organic-intercalated derivatives, Phys. Chem. Miner. **15**, 465 (1988).

[46] S. Calder, K. An, R. Boehler, C. Dela Cruz, M. Frontzek, M. Guthrie, B. Haberl, A. Huq, S. A. Kimber, J. Liu, J. J. Molaison, J. Neuefeind, K. Page, A. M. dos Santos, K. M. Taddei, C. Tulk, and M. G. Tucker, A suite-level review of the neutron powder diffraction instruments at Oak Ridge National Laboratory, Rev. Sci. Instrum. **89**, 092701 (2018).

[47] J. Rodríguez-Carvajal, Recent advances in magnetic structure determination by neutron powder diffraction, Phys. B: Condens. Matter **192**, 55 (1993).

[48] A. Wills, A new protocol for the determination of magnetic structures using simulated annealing and representational analysis (SARA*h*), Phys. B: Condens. Matter **276**, 680 (2000).

[49] M. Aroyo, J. Perez-Mato, C. Capillas, E. Kroumova, S. Ivantchev, G. Madariaga, A. Kirov, and H. Wondratschek, Bilbao Crystallographic Server: I. Databases and crystallographic computing programs, Z. Kristallogr. **221**, 15 (2006).

[50] M. Aroyo, A. Kirov, C. Capillas, J. Perez-Mato, and H. Wondratschek, Bilbao Crystallographic Server. II. Representations of crystallographic point groups and space groups, Acta Crystallogr. Sect. A: Found. Crystallogr. **62**, 115 (2006).

[51] M. I. Aroyo, J. M. Perez-Mato, D. Orobengoa, E. Tasci, G. De La Flor, and A. Kirov, Crystallography online: Bilbao Crystallographic Server, Bulg. Chem. Commun. **43**, 183 (2011).

[52] K. Momma and F. Izumi, *VESTA 3* for three dimensional visualization of crystal, volumetric and morphology data, J. Appl. Crystallogr. **44**, 1272 (2011).

[53] I. A. Zaliznyak, A. T. Savici, V. O. Garlea, B. Winn, U. Filges, J. Schneeloch, J. M. Tranquada, G. Gu, A. Wang, and C. Petrovic, Polarized neutron scattering on HYSPEC: The HYbrid SPECtrometer at SNS, J. Phys.: Conf. Ser. **862**, 012030 (2017).

[54] A. M. Samarakoon, K. Barros, Y. W. Li, M. Eisenbach, Q. Zhang, F. Ye, V. Sharma, Z. Dun, H. Zhou, S. A. Grigera, C. D. Batista, and D. A. Tennant, Machine-learning-assisted insight into spin ice $Dy_2Ti_2O_7$, Nat. Commun. **11**, 892 (2020).

[55] S. Toth and B. Lake, Linear spin wave theory for single-Q incommensurate magnetic structures, J. Phys.: Condens. Matter **27**, 166002 (2015).

[56] P. Blaha, K. Schwarz, G. Madsen, D. Kvasnicka, and J. Luitz, *WIEN2k: An Augmented Plane Wave Plus Local Orbitals Program for Calculating Crystal Properties* (Technische Universität Wien, Vienna, 2001).

[57] J. P. Perdew, K. Burke, and M. Ernzerhof, Generalized Gradient Approximation Made Simple, Phys. Rev. Lett. **77**, 3865 (1996).

[58] V. I. Anisimov, F. Aryasetiawan, and A. Lichtenstein, First-principles calculations of the electronic structure and spectra of strongly correlated systems: the LDA+U method, J. Phys.: Condens. Matter **9**, 767 (1997).

[59] G. Pokharel, A. F. May, D. S Parker, S. Calder, G. Ehlers, A. Huq, S. A. J. Kimber, H. S. Arachchige, L. Poudel, M. A. McGuire, D. Mandrus, and A. D. Christianson, Negative thermal expansion and magnetoelastic coupling in the breathing pyrochlore lattice material $LiGaCr_4S_8$, Phys. Rev. B **97**, 134117 (2018).

[60] J. L. Niedziela, L. D. Sanjeewa, A. A. Podlesnyak, L. DeBeer-Schmitt, S. J. Kuhn, C. de la Cruz, D. S. Parker, K. Page, and A. S. Sefat, Magnetoelastic coupling, negative thermal expansion, and two-dimensional magnetic excitations in FeAs, Phys. Rev. B **103**, 094431 (2021).

[61] L. D. Sanjeewa, J. Xing, K. M. Taddei, D. Parker, R. Custelcean, C. dela Cruz, and A. S. Sefat, Evidence of Ba-substitution induced spin-canting in the magnetic Weyl semimetal $EuCd_2As_2$, Phys. Rev. B **102**, 104404 (2020).

[62] A. F. May, M. A. McGuire, H. Cao, I. Sergueev, C. Cantoni, B. C. Chakoumakos, D. S. Parker, and B. C. Sales, Spin Reorientation in $TlFe_{1.6}Se_2$ with Complete Vacancy Ordering, Phys. Rev. Lett. **109**, 077003 (2012); **109**, 119902(E) (2012) .

[63] K. Shanavas, D. Parker, and D. J. Singh, Theoretical study on the role of dynamics on the unusual magnetic properties in MnBi, Sci. Rep. **4**, 1 (2014).

[64] S. T. Bramwell, A. M. Buckley, and P. Day, The magnetic structure of $KNiAsO_4$: A two-dimensional honeycomb lattice, J. Solid State Chem. **111**, 48 (1994).

[65] Z. Hiroi, M. Hanawa, N. Kobayashi, M. Nohara, H. Takagi, Y. Kato, and M. Takigawa, Spin-1/2 *Kagomé*-Like lattice in Volborthite $Cu_3V_2O_7(OH)_2 \cdot 2H_2O$, J. Phys. Soc. Jpn. **70**, 3377 (2001).

[66] A. Vasiliev, O. Volkova, E. Zvereva, and M. Markina, Milestones of low-D quantum magnetism, npj Quantum Mater. **3**, 18 (2018).

[67] K. M. Taddei, L. D. Sanjeewa, J. Xing, Q. Zhang, D. Parker, A. Podlesnyak, C. dela Cruz, and A. S. Sefat, Tunable magnetic order in low-symmetry SeO_3 ligand linked $TM_3(SeO_3)_3H_2O$ (TM = Mn, Co, and Ni) compounds, Phys. Rev. Mater. **4**, 024410 (2020).

[68] A. Virtue, X. Zhou, B. Wilfong, J. W. Lynn, K. Taddei, P. Zavalij, L. Wang, and E. E. Rodriguez, Magnetic order effects on the electronic structure of $KMMnS_2$(M = Cu, Li) with the $ThCr_2Si_2$-type structure, Phys. Rev. Mater. **3**, 044411 (2019).

[69] S. Pal, S. Sarkar, K. Kumar, R. Raghunathan, R. J. Choudhary, A. Banerjee, and S. B. Roy, Role of electronic excitation on the anomalous magnetism of elemental copper, Phys. Rev. B **105**, L060406 (2022).

[70] Q. Chen, S. Fan, K. M. Taddei, M. B. Stone, A. I. Kolesnikov, J. Cheng, J. L. Musfeldt, H. Zhou, and A. A. Aczel, Large positive zero-field splitting in the cluster magnet $Ba_3CeRu_2O_9$, J. Am. Chem. Soc. **141**, 9928 (2019).

[71] D. Phelan, D. Louca, S. Rosenkranz, S.-H. Lee, Y. Qiu, P. J. Chupas, R. Osborn, H. Zheng, J. F. Mitchell, J. R. D. Copley, J. L. Sarrao, and Y. Moritomo, Nanomagnetic Droplets and Implications to Orbital Ordering in $La_{1-x}Sr_xCoO_3$, Phys. Rev. Lett. **96**, 027201 (2006).

[72] P. Lampen-Kelley, S. Rachel, J. Reuther, J.-Q. Yan, A. Banerjee, C. A. Bridges, H. B. Cao, S. E. Nagler, and D. Mandrus, Anisotropic susceptibilities in the honeycomb Kitaev system $\alpha - RuCl_3$, Phys. Rev. B **98**, 100403(R) (2018).

[73] J. A. Sears, M. Songvilay, K. W. Plumb, J. P. Clancy, Y. Qiu, Y. Zhao, D. Parshall, and Y.-J. Kim, Magnetic order in $\alpha - RuCl_3$: A honeycomb-lattice quantum magnet with strong spin-orbit coupling, Phys. Rev. B **91**, 144420 (2015).

[74] Y. Singh and P. Gegenwart, Antiferromagnetic Mott insulating state in single crystals of the honeycomb lattice material Na_2IrO_3, Phys. Rev. B **82**, 064412 (2010).

[75] K. M. Taddei, L. Yin, L. D. Sanjeewa, Y. Li, J. Xing, C. dela Cruz, D. Phelan, A. S. Sefat, and D. S. Parker, Single pair of Weyl nodes in the spin-canted structure of $EuCd_2As_2$, Phys. Rev. B **105**, L140401 (2022).

[76] K. M. Taddei, L. Sanjeewa, J. W. Kolis, A. S. Sefat, C. de la Cruz, and D. M. Pajerowski, Local-Ising-type magnetic order and metamagnetism in the rare-earth pyrogermanate $Er_2Ge_2O_7$, Phys. Rev. Mater. **3**, 014405 (2019).

[77] J. Xing, K. M. Taddei, L. D. Sanjeewa, R. S. Fishman, M. Daum, M. Mourigal, C. dela Cruz, and A. S. Sefat, Stripe antiferromagnetic ground state of the ideal triangular lattice compound $KErSe_2$, Phys. Rev. B **103**, 144413 (2021).

[78] E. Stavrou, X.-J. Chen, A. R. Oganov, a. F. Wang, Y. J. Yan, X. G. Luo, X. H. Chen, and A. F. Goncharov, Formation of As-As interlayer bonding in the collapsed tetragonal phase of $NaFe_2As_2$ under pressure, Sci. Rep. **5**, 9868 (2015).

[79] J. C. V. Chaloupka, G. Jackeli, and G. Khaliullin, Zigzag Magnetic Order in the Iridium Oxide Na_2IrO_3, Phys. Rev. Lett. **110**, 097204 (2013).

[80] S. K. Choi, R. Coldea, A. N. Kolmogorov, T. Lancaster, I. I. Mazin, S. J. Blundell, P. G. Radaelli, Y. Singh, P. Gegenwart, K. R. Choi, S.-W. Cheong, P. J. Baker, C. Stock, and J. Taylor, Spin Waves and Revised Crystal Structure of Honeycomb Iridate Na_2IrO_3, Phys. Rev. Lett. **108**, 127204 (2012).

[81] T. Halloran, F. Desrochers, E. Z. Zhang, T. Chen, L. E. Chern, Z. Xu, B. Winn, M. Graves-Brook, M. Stone, A. I. Kolesnikov, Y. Qui, R. Zhong, R. Cava, Y. B. Kim, and C. Broholm, Geometrical frustration versus Kitaev interactions in $BaCo_2(AsO_4)_2$, arXiv:2205.15262.

[82] J. G. Rau, E. K.-H. Lee, and H.-Y. Kee, Generic Spin Model for the Honeycomb Iridates beyond the Kitaev Limit, Phys. Rev. Lett. **112**, 077204 (2014).

[83] H. S. Nair, J. M. Brown, E. Coldren, G. Hester, M. P. Gelfand, A. Podlesnyak, Q. Huang, and K. A. Ross, Short-range order in the quantum XXZ honeycomb lattice material $BaCo_2(PO_4)_2$, Phys. Rev. B **97**, 134409 (2018).

[84] C. Balz, B. Lake, A. T. M. Nazmul Islam, Y. Singh, J. A. Rodriguez-Rivera, T. Guidi, E. M. Wheeler, G. G. Simeoni, and H. Ryll, Magnetic Hamiltonian and phase diagram of the quantum spin liquid $Ca_{10}Cr_7O_{28}$, Phys. Rev. B **95**, 174414 (2017).

[85] H. Suzuki, H. Liu, J. Bertinshaw, K. Ueda, H. Kim, S. Laha, D. Weber, Z. Yang, L. Wang, H. Takahashi, K. Fürsich, M. Minola, B. V. Lotsch, B. J. Kim, H. Yavaş, M. Daghofer, J. Chaloupka, G. Khaliullin, H. Gretarsson, and B. Keimer, Proximate ferromagnetic state in the Kitaev model material α-$RuCl_3$, Nat. Commun. **12**, 4512 (2021).

[86] D. A. Tennant, S. E. Nagler, A. W. Garrett, T. Barnes, and C. C. Torardi, Excitation Spectrum and Superexchange Pathways in the Spin Dimer $VODPO_4 \cdot \frac{1}{2}D_2O$, Phys. Rev. Lett. **78**, 4998 (1997).

[87] M. Matsuda, S. E. Dissanayake, D. L. Abernathy, Y. Qiu, J. R. D. Copley, N. Kumada, and M. Azuma, Frustrated magnetic interactions in an $S = 3/2$ bilayer honeycomb lattice compound $Bi_3Mn_4O_{12}(NO_3)$, Phys. Rev. B **100**, 134430 (2019).

[88] B. Gao, T. Chen, C. Wang, L. Chen, R. Zhong, D. L. Abernathy, D. Xiao, and P. Dai, Spin waves and Dirac magnons in a honeycomb-lattice zigzag antiferromagnet $BaNi_2(AsO_4)_2$, Phys. Rev. B **104**, 214432 (2021).

[89] S. Das, S. Voleti, T. Saha-Dasgupta, and A. Paramekanti, XY magnetism, Kitaev exchange, and long-range frustration in the $J_{\text{eff}} = \frac{1}{2}$ honeycomb cobaltates, Phys. Rev. B **104**, 134425 (2021).

[90] K. Y. Chen, B. S. Wang, J.-Q. Yan, D. S. Parker, J.-S. Zhou, Y. Uwatoko, and J.-G. Cheng, Suppression of the antiferromagnetic metallic state in the pressurized $MnBi_2Te_4$ single crystal, Phys. Rev. Mater. **3**, 094201 (2019).

[91] J.-Q. Yan, Y. H. Liu, D. S. Parker, Y. Wu, A. A. Aczel, M. Matsuda, M. A. McGuire, and B. C. Sales, A-type antiferromagnetic order in $MnBi_4Te_7$ and $MnBi_6Te_{10}$ single crystals, Phys. Rev. Mater. **4**, 054202 (2020).

[92] T. Williams, A. Taylor, A. Christianson, S. Hahn, R. Fishman, D. Parker, M. McGuire, B. Sales, and M. Lumsden, Extended magnetic exchange interactions in the high-temperature ferromagnet MnBi, Appl. Phys. Lett. **108**, 192403 (2016).

[93] T. N. Lamichhane, V. Taufour, M. W. Masters, D. S. Parker, U. S. Kaluarachchi, S. Thimmaiah, S. L. Bud'ko, and P. C. Canfield, Discovery of ferromagnetism with large magnetic anisotropy in ZrMnP and HfMnP, Appl. Phys. Lett. **109**, 092402 (2016).

[94] V. V. Klepov, K. A. Pace, A. A. Berseneva, J. B. Felder, S. Calder, G. Morrison, Q. Zhang, M. J. Kirkham, D. S. Parker, and H.-C. zur Loye, Chloride reduction of Mn^{3+} in mild hydrothermal synthesis of a charge ordered defect pyrochlore, $CsMn^{2+}Mn^{3+}F_6$, a canted antiferromagnet with a hard ferromagnetic component, J. Am. Chem. Soc. **143**, 11554 (2021).

[95] G. Qin, W. Ren, and D. J. Singh, Interplay of local moment and itinerant magnetism in cobalt-based Heusler ferromagnets: Co_2TiSi, Co_2MnSi and Co_2FeSi, Phys. Rev. B **101**, 014427 (2020).

[96] http://energy.gov/downloads/doe-public-access-plan.